

RESEARCH ARTICLE

10.1002/2013JB010926

Key Points:

- Depth Extension of 35 km is observed during the rupture of this deep earthquake
- The source process and seismicity cannot be explained by one or two planes
- The results favor a cascading triggering of shear instabilities

Supporting Information:

- Readme
- Tables S1–S6 and Figures S1–S7

Correspondence to:

Y. Chen,
Yu.Chen@stonybrook.edu

Citation:

Chen, Y., L. Wen, and C. Ji (2014), A cascading failure during the 24 May 2013 great Okhotsk deep earthquake, *J. Geophys. Res. Solid Earth*, 119, doi:10.1002/2013JB010926.

Received 20 DEC 2013

Accepted 28 FEB 2014

Accepted article online 10 MAR 2014

A cascading failure during the 24 May 2013 great Okhotsk deep earthquake

Yu Chen¹, Lianxing Wen^{1,2}, and Chen Ji³

¹Department of Geosciences, State University of New York at Stony Brook, Stony Brook, New York, USA, ²Laboratory of Seismology and Physics of Earth's Interior, University of Science and Technology of China, Hefei, China, ³Department of Earth Science, University of California, Santa Barbara, California, USA

Abstract On 24 May 2013, the largest ever-recorded deep earthquake occurred beneath Sea of Okhotsk. A multiple point source inversion procedure is applied to constrain source process of this earthquake, based on waveform modeling of both direct *P* and *SH* waves and near-surface reflected *pP* and *sSH* waves. Our results indicate that the earthquake consists of six major subevents separated in space and time, encompassing a horizontal dimension of 64 ± 4 km along $\sim N160^\circ E$ and a downward depth extension of 35 ± 4 km. The geographic distribution and focal mechanisms of the inferred subevents and foreshock/aftershock locations do not fit into plane rupture. We suggest that the earthquake can be best explained by a cascading failure of shear instability within preexisting weak zones in the region, with the perturbation of stress generated by a shear instability triggering another.

1. Introduction

The occurrence of deep-focus earthquakes remains enigmatic, because the pressure in the upper mantle would strongly inhibit brittle failure, and the temperature would result in ductile deformation [Scholz, 2002]. Three physical mechanisms have been put forward, including dehydration embrittlement [Jung *et al.*, 2004; Meade and Jeanloz, 1991], shear thermal instability [Green, 2007; Hobbs and Ord, 1988; Kanamori *et al.*, 1998; Kelemen and Hirth, 2007; Meade and Jeanloz, 1989; Ogawa, 1987], and transformational faulting [Green and Houston, 1995; Kirby, 1987; Kirby *et al.*, 1996; Wiens *et al.*, 1993].

Studies of the source processes and aftershock distributions of major deep earthquakes provided important constraints on deep earthquake mechanisms. For example, seismic studies of the 1994 *Mw* 8.2 Bolivia earthquake, the largest deep earthquake before the occurrence of 2013 *Mw* 8.3 Okhotsk earthquake, suggested a large subhorizontal fault plane with its lateral extension exceeding the width of the metastable olivine [Antolik *et al.*, 1996; Silver *et al.*, 1995; Zhan *et al.*, 2014]. The study of seismic efficiency of that earthquake also proposed possible melting during the earthquake [Kanamori *et al.*, 1998]. The aftershock sequence of the 1994 *Mw* 7.6 Tonga deep earthquake suggested rupture propagating in a direction normal to the expected metastable olivine wedge and over a distance too large to fit within the expected dimensions of the wedge [Wiens *et al.*, 1994]. On the other hand, some studies have suggested seismological evidence for the existence of metastable olivine wedge [Wiens *et al.*, 1993]. And the observations of a broad peak in seismicity between 300 and 530 km [Estabrook, 2004] and major deep-focus earthquake moment releasing in the slab core [Antolik *et al.*, 1999] have been suggested as evidences that the transformational faulting may play an important role in cold slab.

The 24 May 2013 deep earthquake occurred beneath Sea of Okhotsk, with a moment magnitude of *Mw* 8.3 in the Global Centroid Moment Tensor (GCMT) solution and a hypocenter depth of 598 km reported by the United States Geological Survey (USGS). The earthquake is also reported to have a subhorizontal rupture with a great dimension [Wei *et al.*, 2013; Zhan *et al.*, 2014], low stress drop, and a heterogeneous rupture with preexisting weak zone [Ye *et al.*, 2013]. However, only direct *P* wave observations have been used in these studies to constrain the rupture process of this earthquake. In this study, we constrain the source process of this earthquake based on waveform modeling of direct *P* and *SH* waves and near-surface reflected *pP* and *sSH* waves. Using all these types of seismic waves allows the source process of this earthquake to be better constrained, especially the depth extent of seismic energy propagation. In fact, our results would show that the earthquake rupture does not fit into a single plane. We present seismic data processing in section 2, seismic source directivity in section 3, source model based on multiple source inversion in section 4, relationship with foreshocks/aftershocks in section 5, model resolution tests in section 6, and our preferred physical mechanism in section 7.

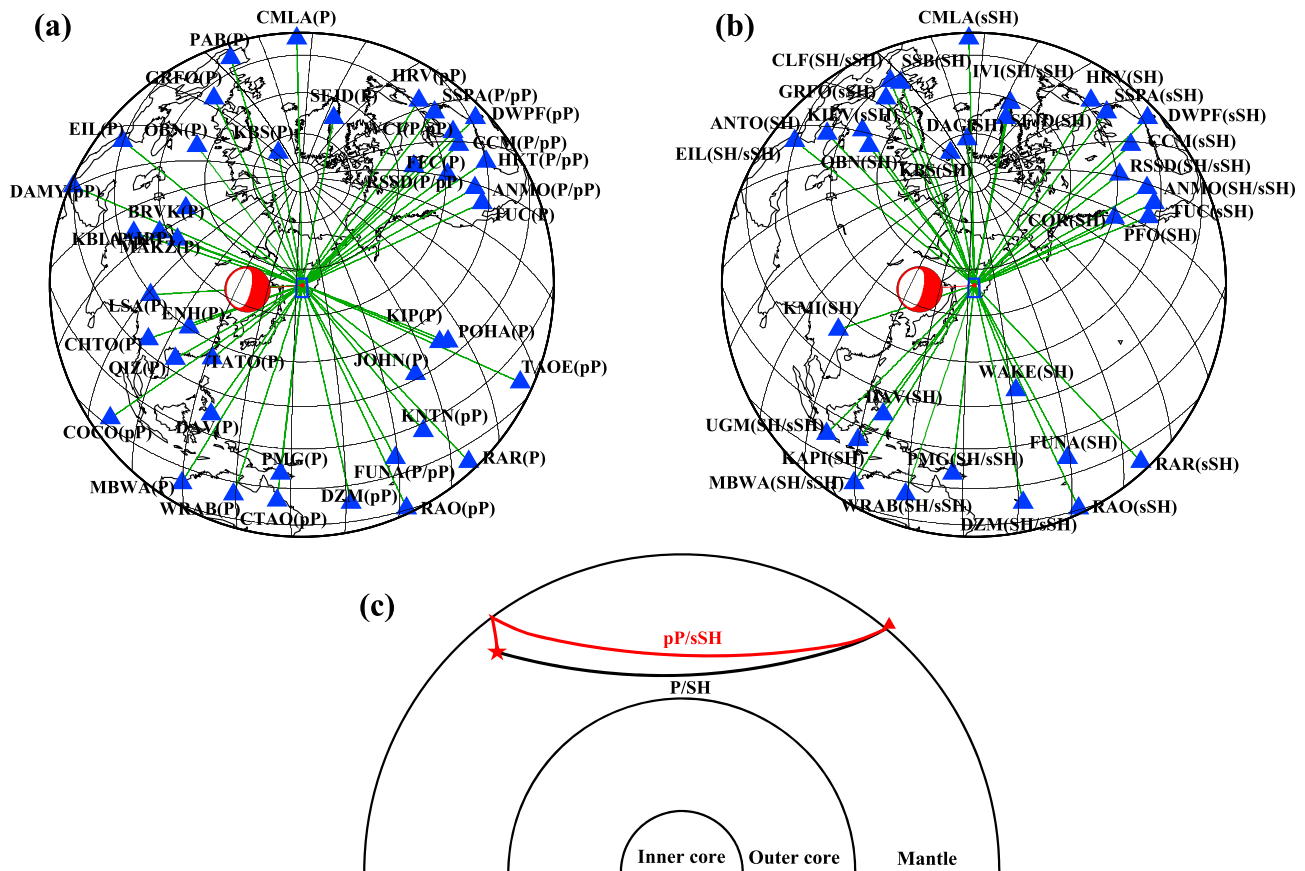


Figure 1. Location of the 24 May 2013 earthquake (red dots) and seismic coverage of (a) *P* and *pP* waves and (b) *SH* and *sSH* waves. Blue triangles represent seismic stations, labeled with station name and seismic phase used. Blue rectangle is the studied area with the seismic result presented in Figure 5. Red beach balls describe GCMT focal mechanism of the main shock. (c) Raypaths for direct phases *P/SH* (black path) and near-surface reflected phases *pP/sSH* (red path) from earthquake source (star) to a seismic station (triangle) at an epicentral distance of 80°.

2. Seismic Data Processing

The earthquake is well recorded by the Global Seismographic Network (GSN). A total of 33 broadband compressional wave (*P*), 17 near-surface reflected compressional wave (*pP*), 24 transversally polarized shear wave (*SH*), and 19 near-surface reflected transversally polarized shear wave (*sSH*) observations recorded at teleseismic distances between 30° and 90° are selected (Figures 1a, 1b, and raypaths in Figure 1c). The selected data constitute good azimuthal coverage. As we will show, the combination of direct *P* and *SH* waves with the near-surface reflected phases *pP* and *sSH* (Figure 1c) places tight constraints on the depth extent of seismic energy propagation. The displacement seismograms are deconvolved with their respective instrument responses and band pass filtered between 0.01 and 4 Hz.

We align broadband *P* phases by the first-arrival onsets, which can be clearly identified and picked in the data high-pass filtered above 1 Hz. *S*, *pP*, and *sS* phases are aligned iteratively in the inversion process: we first pick them based on IASP91 model [Kennett and Engdahl, 1991] and perform a preliminary inversion with *P* wave heavily weighted over other phases. The alignments of *pP*, *S*, and *sS* phases are adjusted based on the best match between synthetics and data during the inversions.

3. Seismic Source Directivity

The propagation of seismic energy can be inferred from the seismic data, with the lateral direction and distance from the observed azimuthal waveform variation of *P* waves (Figure 2), and the vertical extension

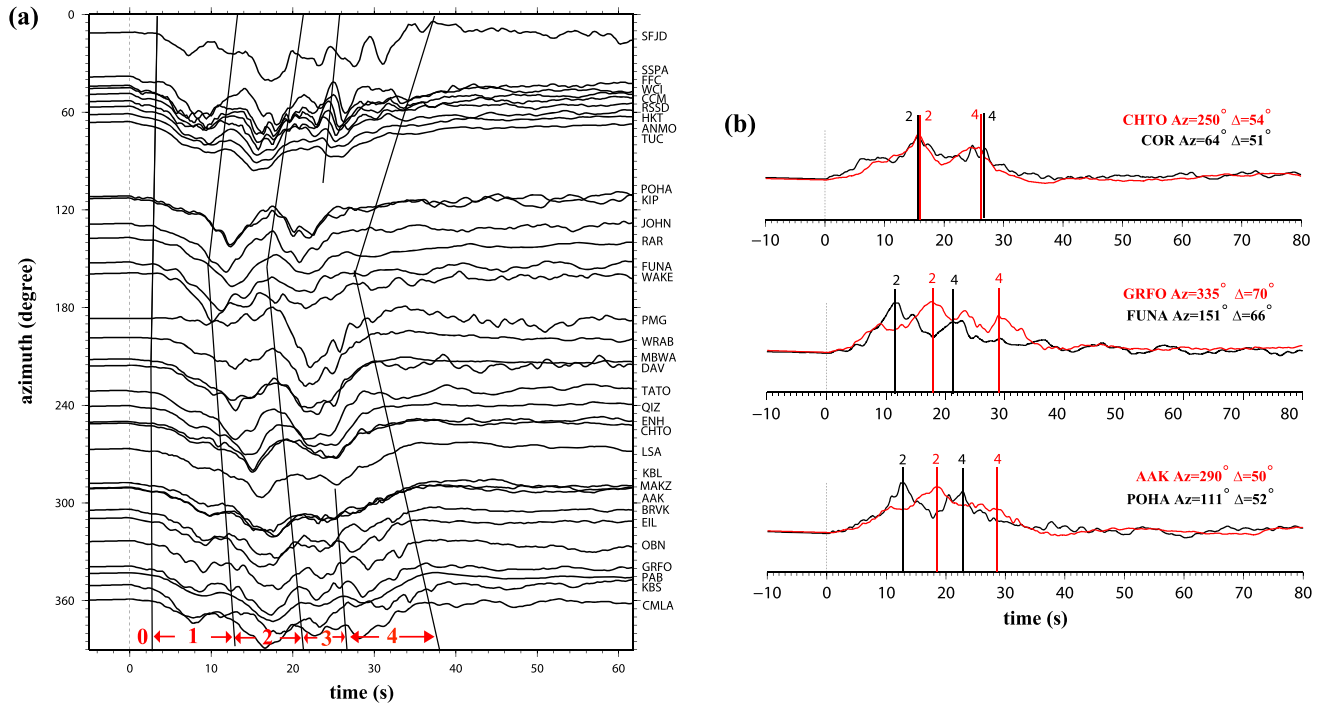


Figure 2. (a) Observed vertical *P* displacement seismograms as a function of azimuth. Black lines divide the seismograms into four major energy pulses (labeled 1–4) and an initiation phase (labeled 0). Seismograms are aligned along the arrival onsets ($t = 0$ s), handpicked from their high-frequency counterparts. (b) Overlays of *P* displacement seismograms observed at three station pairs in roughly opposite azimuths: (1) COR ($Az = 64^\circ$) versus CHTO ($Az = 250^\circ$), (2) FUNA ($Az = 151^\circ$) versus GRFO ($Az = 335^\circ$), and (3) POHA ($Az = 111^\circ$) versus AAK ($Az = 290^\circ$). Seismic records are labeled with station name along with azimuth (Az) and epicentral distance (Δ). Energy pulses are marked in accordance with those in Figure 2a. For display purpose, the polarities of some records have been flipped.

and distance from jointly modeling the *P* and *pP* waves (Figure 3). Using a plane wave approximation, the duration of the *P* or *pP* wave pulse observed at a station can be represented as follows:

$$T(Az, \Delta) = T_r - \delta L \cdot \cos(\theta - Az) \cdot P(\Delta) - \delta H \cdot \sqrt{\frac{1}{v^2} - p^2(\Delta)} \quad (1)$$

where Az and Δ represent the azimuth and epicenter distance relative to the station, v the *P* wave velocity in the source region, and T_r rupture duration; δL and δH the horizontal and depth offsets of the rupture, θ the horizontal direction of the rupture, and p the horizontal slowness of *P* or *pP* wave.

The earthquake begins with a small amplitude phase with a duration of about 5 s, followed by strong moment release lasting 30 s. The observed *P* wave waveforms exhibit a strong azimuthal variation with four groups of major energy pulses during the strong moment release, discernible with different moveouts (time windows labeled 1 to 4, Figure 2a). The azimuthal variation of the *P* wave data indicates that the seismic energy propagates along $\sim N160^\circ E$ (the azimuth with the shortest duration of the *P* wave waveforms, Figure 2a). The directivity can also be clearly seen from data pairs at different azimuths. We select three pairs of *P* wave data observed at similar epicentral distances but at opposite direction from the source (Figure 2b). The first pair of *P* observations is from stations COR and CHTO roughly normal to the $N160^\circ E$ direction; both observations exhibit similar arrival times for all major pulses (top pair, Figure 2b). The second pair is from stations FUNA and GRFO roughly parallel to $N160^\circ E$. The arrival time differences of each group of energy almost reach the maximum in these opposite azimuths (middle pair, Figure 2b). The third pair is from stations POHA and AAK oblique to the $N160^\circ E$ direction but roughly perpendicular to the strikes of GCMT nodal planes (13° or 191°). Each of the major groups of energy arrives earlier at station POHA (bottom pair, Figure 2b). The azimuthal variations of the *P* wave data clearly indicate a lateral propagation of seismic energy along an azimuth of $\sim 160^\circ$. It is also clear that the third group of energy exhibits a smaller moveout with respect to those of the second and fourth groups of energy, indicating that the third group of energy propagates backward to the opposite direction (Figure 2a).

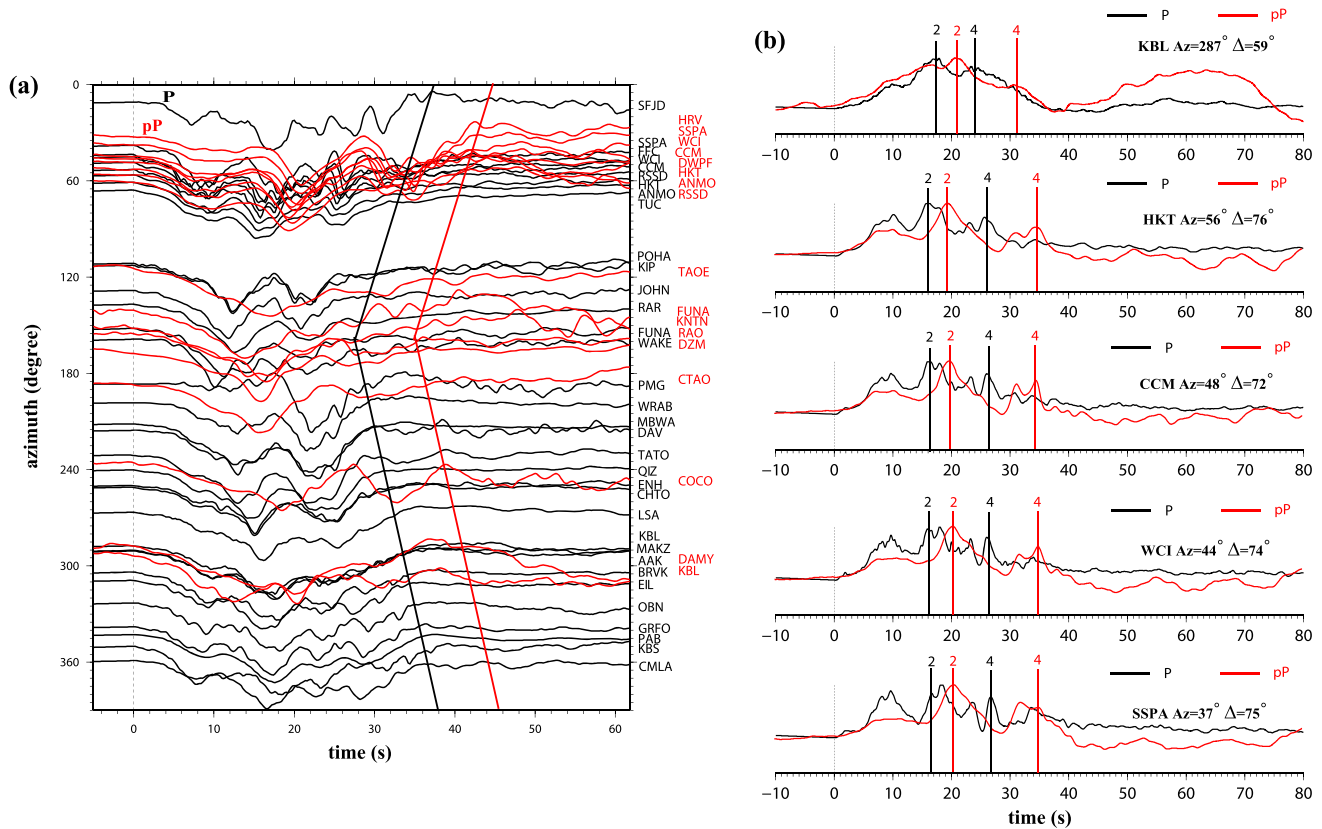


Figure 3. (a) Comparison of observed P (black) and pP (red) displacement seismograms as a function of azimuth. The black and red lines indicate the ending time of P and pP data, respectively. (b) Overlays of P (black) and pP (red) displacements observed at five stations: KBL, HKT, CCM, WCI, and SSPA. Seismic records are labeled with station name along with azimuth (Az) and epicentral distance (Δ). The black and red lines mark the maximal of the second and fourth groups of energy labeled in Figure 2a. For display purpose, the polarities of some records have been flipped.

The pP waveforms exhibit similar azimuthal variation as the P waveforms (Figure 3a), corroborating the inferred lateral propagation direction of various groups of energy based on the observed P waveforms. However, major groups of energy are delayed in pP waveforms than in P waveforms, and the duration of pP waveforms is about 7–8 s longer (Figure 3a). We show five example pairs of P and pP seismograms observed at stations KBL, HKT, CCM, WCI, and SSPA, to further illustrate this feature (Figure 3b). Two reference times are marked in Figure 3b, corresponding to the peaks of the second and fourth energy pulses in Figure 2a. The second and fourth pulses exhibit 3–4 s and 7–8 s delays in pP waveforms than in P waveforms, respectively. The positive delays of different groups of energy observed in the pP waveforms than in P waveforms indicate that the propagation of energy goes deeper, as a deeper source would make seismic energy arrive later in pP than in P . A 3–4 s delay of the second pulse and a 7–8 s delay of the fourth pulse in pP waveforms correspond to that the sources of the second and fourth pulses are about 15–20 km and 35–40 km deeper than the earthquake initiation point, respectively.

4. Source Model Based on Multiple Source Inversion

We develop a multiple point source inversion procedure to infer the source process of the earthquake. The multiple source inversion method treats the large earthquake as a combination of multiple double couple sources (subevents) separated in space and time. The inversion resolves the spatiotemporal separation and focal mechanism of each subevent based on waveform fitting the seismic data. Each subevent is represented by nine parameters: strike; dip and slip for focal mechanism; dt for time separation of origin time from the initiation; de , dn , and dz for distance separations from the initiation in east, north, and z direction, respectively, seismic moment and source duration. The synthetic seismograms are computed by the Generalized Ray Theory method [Helmberg, 1968], based on the velocity and attenuation structures of PREM (preliminary

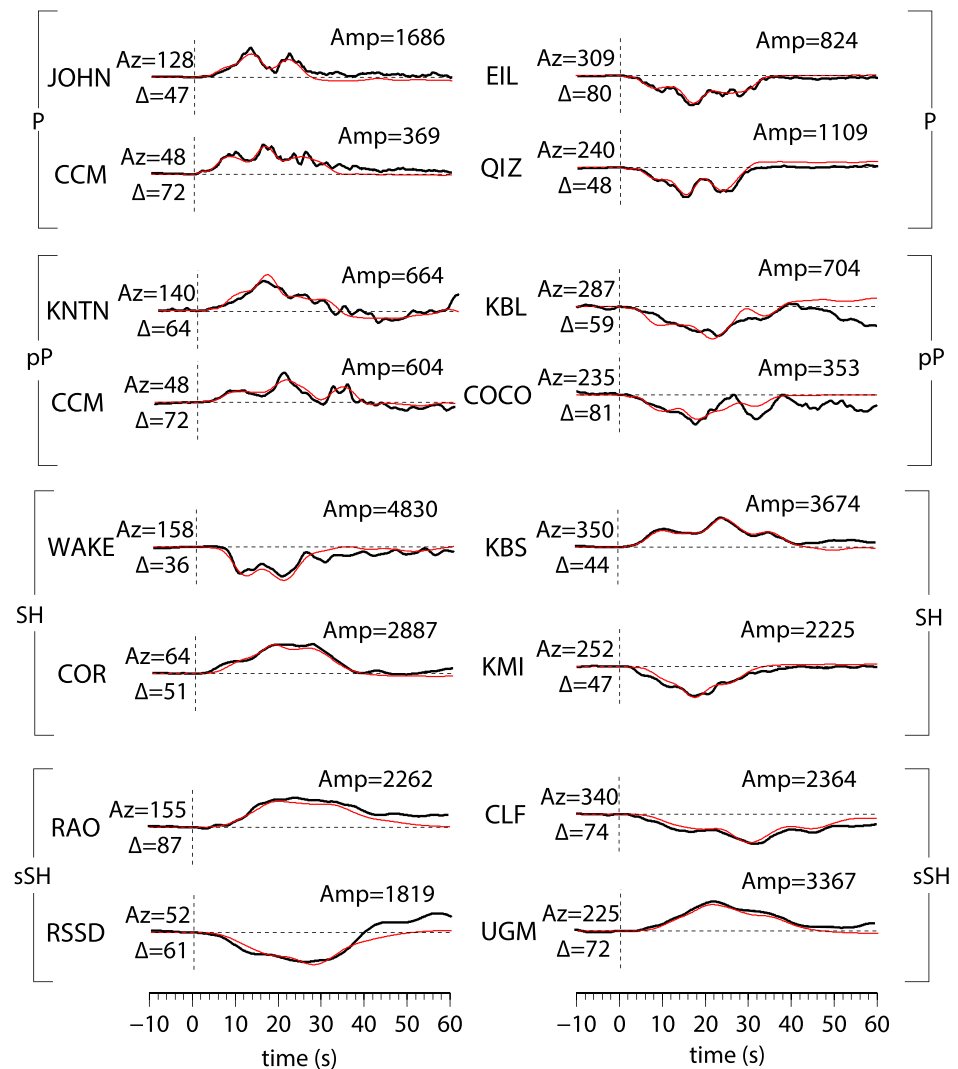


Figure 4. Selected seismograms (black traces) comparing with synthetics (red traces) predicted based on the inverted six subevent model (Table 1) in four quadrants for *P* phase (vertical displacement), *pP* phase (vertical displacement), *SH* phase (tangential displacement), and *sSH* phase (tangential displacement). Seismic records are labeled with station name along with azimuth (*Az*), epicentral distance (Δ), and the maximum amplitude (*Amp*) of the data. The unit of the amplitude is 10^{-6} m. The whole waveform fitting of all used stations is shown in Figure S1.

reference Earth model) [Dziewonski and Anderson, 1981]. The $9 \times N$ (N , number of subevents) inversion parameters are searched by the simulated heat-annealing algorithm [Ji et al., 2002] for the best fitting model with the smallest misfit (root-mean-square, RMS) between the data and synthetics.

Because the multiple source inversion is nonlinear, we adopt a two-step inversion procedure. We first perform the inversion with four subevents that correspond to groups of major energy in the observed seismograms. We then refine the data fitting with a six subevent inversion and narrow down the search parameter ranges based on the four subevent inversion results. In the first four subevent inversion, we first roughly estimate the source parameters based on seismic observations: dt from the average arrival times of each pulse in Figures 2a and 3a, dn and de from the moveout slowness of each pulse in Figure 2a, dz from the differences of arrival times between *P* and *pP* in Figure 3a, and the duration and moment from visual inspection of wave shapes and amplitudes. We then search the best fitting parameters centered at those initial estimates. The search focal parameters are $\pm 30^\circ$ from the GCMT subvertical plane. The searching ranges for other parameters are ± 3 s for dt ; ± 30 km for dn , de , and dz ; and $\pm 50\%$ for source durations and moments. In the second step of six-event inversion, we add subevent 0 for the weak initiation onset and

Table 1. Source Parameters of Inverted Six Subevents of 24 May 2013 Earthquake

| Subevent | <i>dt</i> (s) | <i>dn</i> (km) | <i>de</i> (km) | <i>dz</i> (km) | Duration (s) | Moment (dyn cm) | Strike (deg) | Dip (deg) | Slip (deg) |
|----------|---------------|----------------|----------------|----------------|--------------|-----------------|--------------|-----------|------------|
| 0 | 0 | 0 | 0 | 0 | 3 | 3.0E+26 | 8.9 | 87.7 | 278.0 |
| 1a | 1.7 | 4.3 | 4.6 | 1.1 | 12.0 | 6.8E+27 | 13.7 | 85.2 | 278.1 |
| 1b | 7.8 | -6.2 | 8.5 | 0.1 | 12.0 | 6.6E+27 | 23.3 | 86.6 | 263.6 |
| 2 | 12.0 | -44.9 | 15.7 | 16.7 | 9.0 | 7.4E+27 | 4.0 | 76.3 | 282.3 |
| 3 | 16.2 | -21.8 | 10.1 | 4.2 | 11.8 | 8.2E+27 | 17.6 | 85.4 | 256.4 |
| 4 | 22.5 | -57.8 | 15.4 | 35.4 | 12.0 | 7.9E+27 | -5.7 | 69.5 | 272.4 |

split subevent 1 into two for better fitting directivity of the first main pulse (Figure 2a). The search ranges for the parameters of the six subevents are $\pm 30^\circ$ for focal parameters; ± 2 s for *dt*; ± 20 km for *dn*, *de*, and *dz*; and $\pm 50\%$ for source durations and moments, based on the inversion result of the first step.

The inversion results in excellent waveform fitting between synthetics and seismic data for *P*, *pP*, *SH*, and *sSH* waves (Figures 4 and S1 in the supporting information). The inverted best fitting six subevents are shown in Table 1 and Figure 5. The inverted source region has a horizontal extension of 64 km and a depth extension of 35 km. Subevents 2–4 propagate downward along an azimuth of 155° – 165° , while subevents 1a and 1b exhibit bilateral propagation to northeast and southwest, respectively (Figure 5). Subevent 2 has a duration of 9 s and a peak moment rate at 16.5 s (origin time of the subevent from the initiation plus half duration of the subevent). And it is located about 45 km S160°E and 17 km down from the epicenter. Subevent 3 has a duration of 12 s and a peak moment rate at 22 s, and it is located between subevents 1 and 3, 24 km S155°E and 4 km deeper from the epicenter. Subevent 4 is 58 km S165°E and 35 km deeper from the epicenter, with a duration of 12 s and a peak moment rate at 28.5 s. The focal parameters of subevents 1–4 deviate about 20° from the GCMT solution. The focal mechanism of subevent 0 is not well resolved, due to its moment release being at least 1 order of magnitude smaller than other subevents. The summation of the focal mechanisms of the inferred subevents yields an overall focal mechanism of 10/80/270 (strike/dip/slip), similar to that reported for the main shock in the GCMT solution (13/79/270). The predicted total moment is 3.7×10^{28} dyn cm, slightly lower than 4.1×10^{28} dyn cm in the GCMT solution.

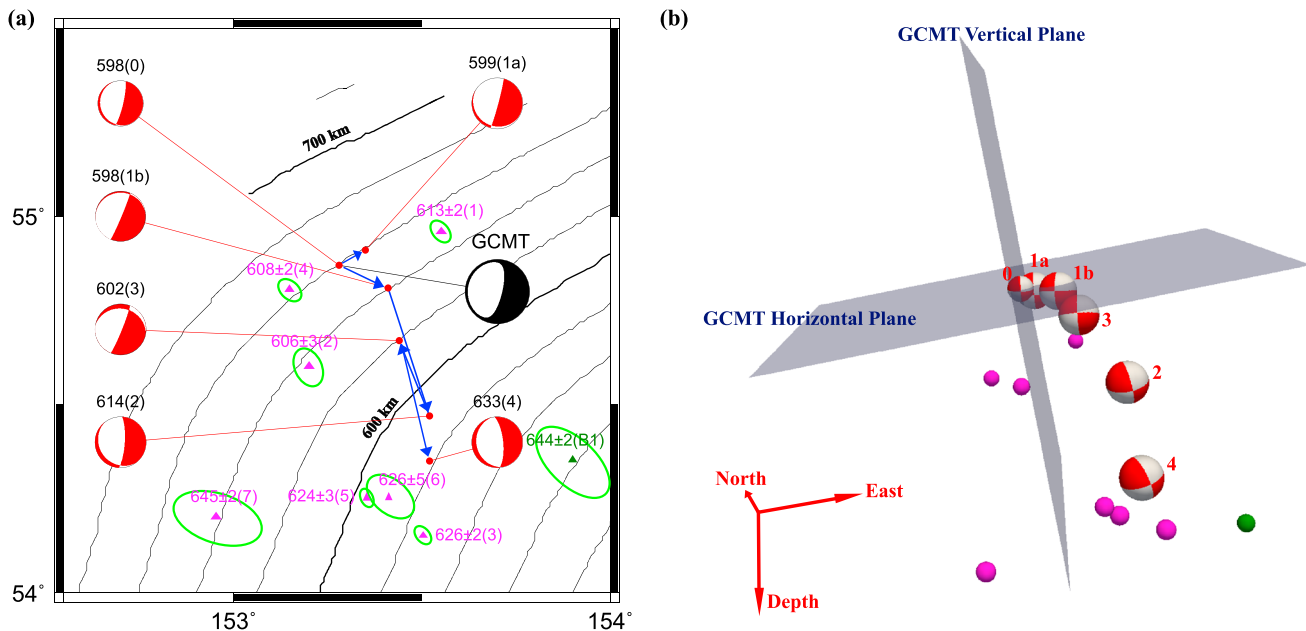


Figure 5. (a) Locations of subevents (red points), aftershocks (purple triangles), and background seismicity (green triangle), along with slab depth contours (black traces, labeled with slab depth). Black beach ball describes GCMT focal mechanism of the main shock. Red beach balls represent inverted focal mechanisms of the subevents, labeled with subevent depth and the occurring sequence number as defined in Figure 2a. Subevents are connected by blue arrows following the sequence of their occurring times. Green ellipses represent the 95% confidence levels of the relocated foreshocks/aftershocks. Subevents, aftershocks, and background seismicity are labeled with depth, depth uncertainty, and sequence number in Tables 1 and 2. Slab depth contours are from the USGS Slab 1.0 model [Hayes et al., 2012]. (b) Three-dimensional spatial distribution and focal mechanisms of inverted subevents (red beach balls) labeled with sequence of their occurring times, along with the focal planes (gray planes) in the GCMT solution. Purple and green spheres represent the foreshocks/aftershocks in Figure 5a.

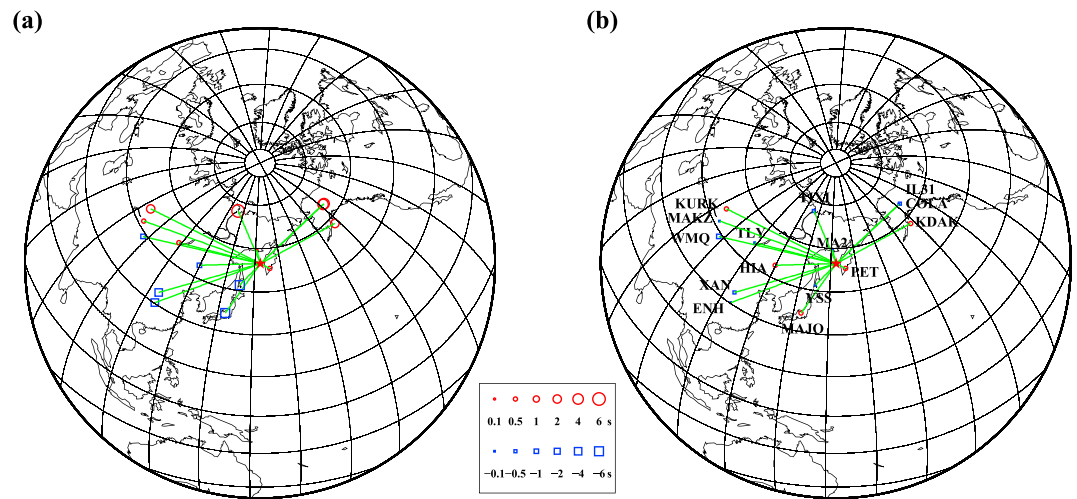


Figure 6. (a) Measured difference in absolute arrival time (circles and squares) of the *P* phases (with respect to their mean) between the main shock and one aftershock 201305241456, plotted centered at the location of each station, along with the great circle paths (green traces) from the main shock (star) to the stations (labeled with station name in Figure 6b). (b) Same as Figure 6a, except that traveltime residuals between the two events are corrected using the best fitting relative location (Table 2).

5. Relationship With Aftershocks and Background Seismicity

We use a relocation method [Wen, 2006] to determine the locations of the aftershocks and background seismicity relative to the main shock. The method uses the arrival time difference of a particular seismic phase between a waveform doublet, defined as a pair of seismic events occurring at different times but in close location. Because the events occur very close in location, the relative traveltimes are sensitive primarily to the relative change of event location.

We use the differential traveltimes of *P* and *pP* waves recorded at the GSN stations at the distance ranges less than 45° for relocation. The seismic stations constitute good azimuthal coverage between 220° and 60° , but only one station PET is available in other azimuths. A weight is assigned to keep balance with the azimuthal coverage. We are also able to pick *pP* phase for events 1, 7, and B1. The depths of these events are relocated using *P* and *pP* traveltimes with respect to those of the main shock. Each of the aftershock relocations has at least eight station pairs with four-quadrant coverage.

The *Mw* 8.3 main shock is used as the master event, with its location fixed to that reported in the USGS catalog. The search region for the relative locations of the aftershocks is 3° (latitude) \times 3° (longitude) \times 200 km (depth) centered in the main shock location. The search grid intervals are 0.05° in latitude, 0.05° in longitude, and 2 km in depth. The best fitting location and origin time significantly reduce the root-mean-square (RMS) traveltime residual (Figures 6a and 6b).

We relocate eight foreshocks/aftershocks with *Mb* > 4.0 based on the preliminary determination of epicenters bulletin by USGS (Table 2 and Figure 5). The aftershock locations further support the inference that the 24 May 2013 Okhotsk earthquake is not a rupture on a single fault plane. The scattered aftershocks do not fall into the same region of the subevents or fit into a possible plane, neither is the one only small earthquake occurring in the region before the main shock (Figure 5).

6. Resolution Tests

6.1. Resolvability of Subevents

We perform model resolution tests with a synthetic earthquake. We use our expected source model (Table 1) and the station distribution (Figures 1a and 1b) for the Okhotsk earthquake. Noise is added to the synthetics, taken from the observed noise before the earthquake and normalized to 5% maximum amplitude of the synthetic waveforms similar to the noise level in the seismic data. The inverted model is presented in Table S1,

Table 2. Locations of Aftershocks and Background Seismicity^a

| ID | Date | Time | Mb ^c | No. | Before Relocation | | | After Relocation | | |
|----|-----------|----------|-----------------|-----|-------------------|----------|------------|------------------|----------|------------------|
| | | | | | Lon (°E) | Lat (°N) | Depth (km) | Lon (°E) | Lat (°N) | Depth (km) |
| 1 | 5/24/2013 | 07:32:04 | 4.3 | 9 | 153.56 | 54.95 | 602 | 153.55 | 54.95 | 613 ^b |
| 2 | 5/24/2013 | 12:35:00 | 4.1 | 8 | 153.17 | 54.53 | 606 | 153.20 | 54.60 | 606 |
| 3 | 5/24/2013 | 14:33:24 | 4.1 | 8 | 153.50 | 54.11 | 625 | 153.50 | 54.15 | 626 |
| 4 | 5/26/2013 | 12:40:59 | 4.1 | 8 | 153.14 | 54.81 | 599 | 153.15 | 54.80 | 608 |
| 5 | 5/28/2013 | 08:58:39 | 4.4 | 15 | 153.40 | 54.24 | 627 | 153.35 | 54.25 | 624 |
| 6 | 6/5/2013 | 23:29:44 | 4.0 | 8 | 153.35 | 54.27 | 621 | 153.40 | 54.25 | 626 |
| 7 | 6/11/2013 | 10:56:38 | 4.8 | 15 | 152.99 | 54.14 | 642 | 152.95 | 54.20 | 645 ^b |
| B1 | 5/24/2000 | 15:42:57 | 4.4 | 18 | 153.42 | 54.55 | 572 | 153.90 | 54.35 | 644 ^b |

^aID is sequence number of aftershocks and background seismicity. No. is the number of stations used in relocation.

^bDepth relocated using *pP* phase.

^cBodywave Magnitude.

and the waveform fitting is shown in Figure S2. In the test, the starting parameters are estimated based on the directivity analysis as in section 3, and their searching ranges are as follows: strike, dip, and slip are within $\pm 30^\circ$; dt within ± 2 s; and de , dn , and dz within ± 20 km from the test model. The bounds for source duration and moment are 50% deviated from the test model.

The inversion results show that the inversion procedure can recover the focal mechanisms and locations of subevents 1–4 (Tables 1 and S1). The uncertainty is $\pm 2^\circ$ for each focal parameter, ± 0.5 s for dt , and ± 4 km for location. The procedure also recovers the total moment to be 3.53×10^{28} dyn cm, 5% lower than 3.71×10^{28} dyn cm of the test model. The obtained moments for the individual subevent trade off each other because the energy of those subevents overlaps in time at most of the stations. Our inversion results further indicate that the focal mechanism of the first initiation subevent (subevent 0) has a larger error, as its energy is at least 1 order of magnitude smaller than the others.

6.2. Single-Plane Rupture Model Test

The spatial distribution of the inverted subevents indicates that the energy release of this event does not follow a particular plane of rupture. We perform further inversion tests to check if the fitting of seismic data can be compromised with rupture along a particular plane. We perform tests for possible plane rupture of the earthquake for three possible planes: the GCMT subhorizontal plane, the GCMT subvertical plane, and a plane that best connects the inferred subevent locations (Table 1) from the multiple source inversion.

Our first test is to adopt the GCMT subhorizontal focal plane. The locations and focal mechanisms of subevents are inverted on a plane with a strike of 191.0° and a dip of 11.2° , corresponding to the GCMT subhorizontal plane (Figure 7a and Table S2). The most notable misfits are late arrivals in direct *P* and *S* phases and early arrivals in near-surface reflected *pP* and *sS* phases marked with black arrows in Figures 7b and S3. In the direction of inferred lateral rupture propagation, the subhorizontal plane rupture would require the rupture to be up going, rather than down going as required from the comparison of *P* and *pP* data (Figure 3).

It should be pointed out that it is crucial to combine both *P* and *pP* observations in the inversion of source process. The direct teleseismic *P* or *SH* observations have poor resolution in resolving the depth of the propagating energy, as the depth has strong trade-offs with origin time.

We demonstrate these points by performing a synthetic test using the constraints of *P* waves only and prescribing the subevents on the GCMT subhorizontal plane. In this inversion, subevents 1–3 propagate up going along southeast and subevent 4 propagates to south/southwest in horizontal direction (Figure 8a and Table S3). The inverted model predicts *P* synthetics that fit the data equally well as the best fitting model (Figures 8b and S4a). In other words, using the constraints of only *P* wave cannot distinguish our best fitting model from a plane rupture on a GCMT subhorizontal plane. However, the *pP* waveforms predicted by this plane rupture model misfit the data at all the stations, with all groups of energy arriving much earlier in synthetics than in the data (Figures 8b and S4b). Same is also true for *sS* waveforms at stations RAR, RAO, UGM, EIL, KIEV, and GRFO (Figure S4d). This is due to the fact that the subevents are prescribed to move shallower on the GCMT subhorizontal plane.

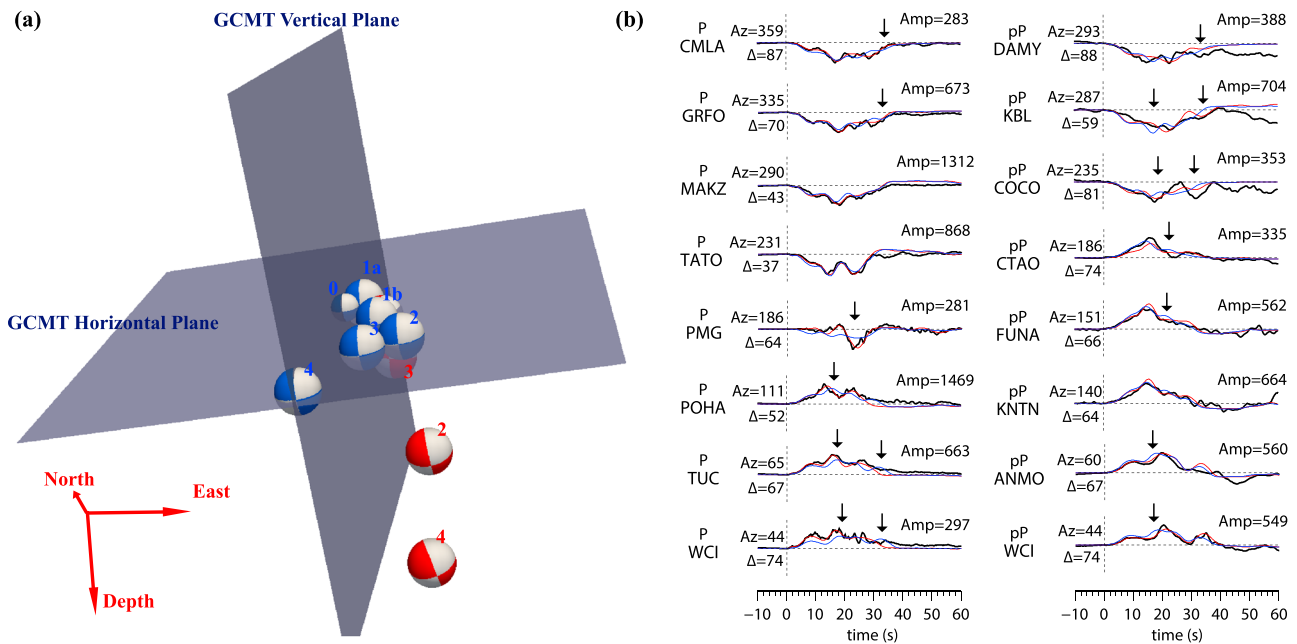


Figure 7. (a) Three-dimensional spatial distribution of focal mechanisms of the best fitting model (red beach balls) and the inverted model of compelling the subevents on the GCMT subhorizontal plane (blue beach balls) labeled with sequence of their occurring time, along with the focal planes (gray planes) in the GCMT solution. (b) Selected seismograms (black traces) comparing with synthetics (red traces) predicted by the best fitting source model (Table 1, red beach balls in Figure 7a) and synthetics (blue traces) predicted by the best fitting source model (Table S2, blue beach balls in Figure 7a) on the GCMT subhorizontal plane. Arrows point to the misfits of the blue traces. The waveform fitting of all used stations is shown in Figure S3.

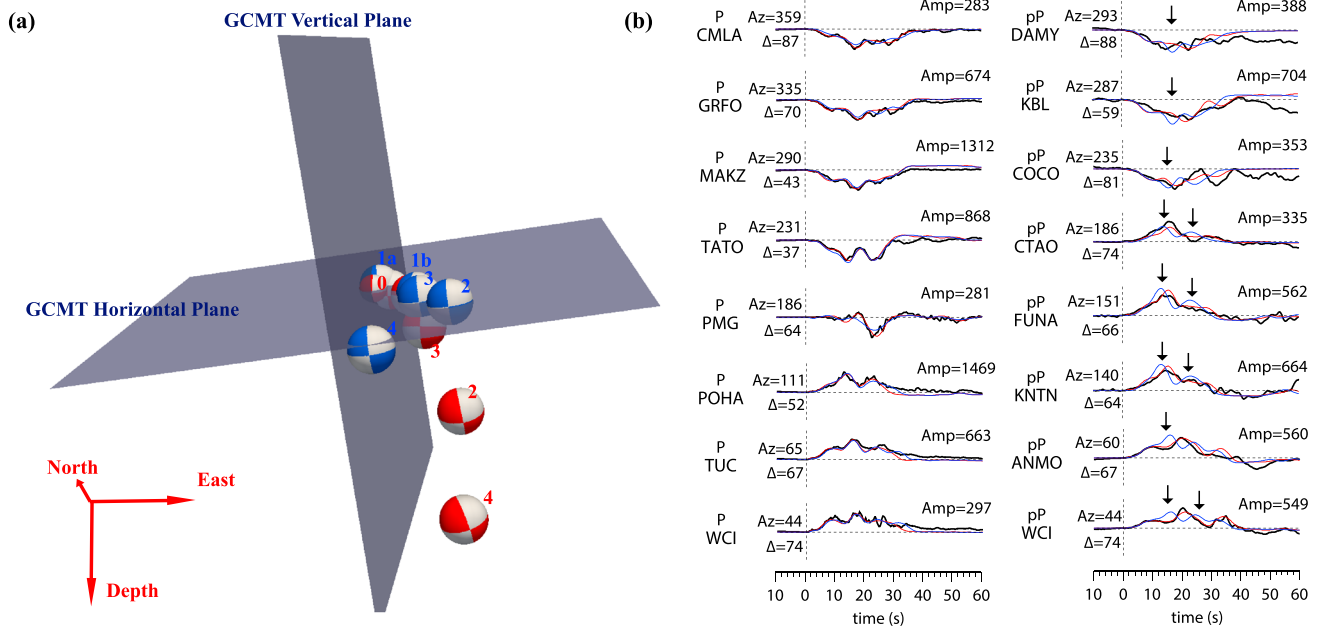


Figure 8. (a) Three-dimensional spatial distribution of focal mechanisms of the best fitting model (red beach balls) and the inverted model of compelling the subevents on the subhorizontal plane (blue beach balls) based on the constraints of *P* wave only, labeled with sequence of their occurring time, along with the focal planes (gray planes) in the GCMT solution. (b) Selected seismograms (black traces) comparing with synthetics (red traces) predicted by the best fitting source model (Table 1, red beach balls in Figure 8a) and synthetics (blue traces) predicted by the best fitting source model (Table S3, blue beach balls in Figure 8a) on the GCMT subhorizontal plane based on *P* wave data only. Arrows point to the misfits of the blue traces. The waveform fitting of all used stations is shown in Figure S4.

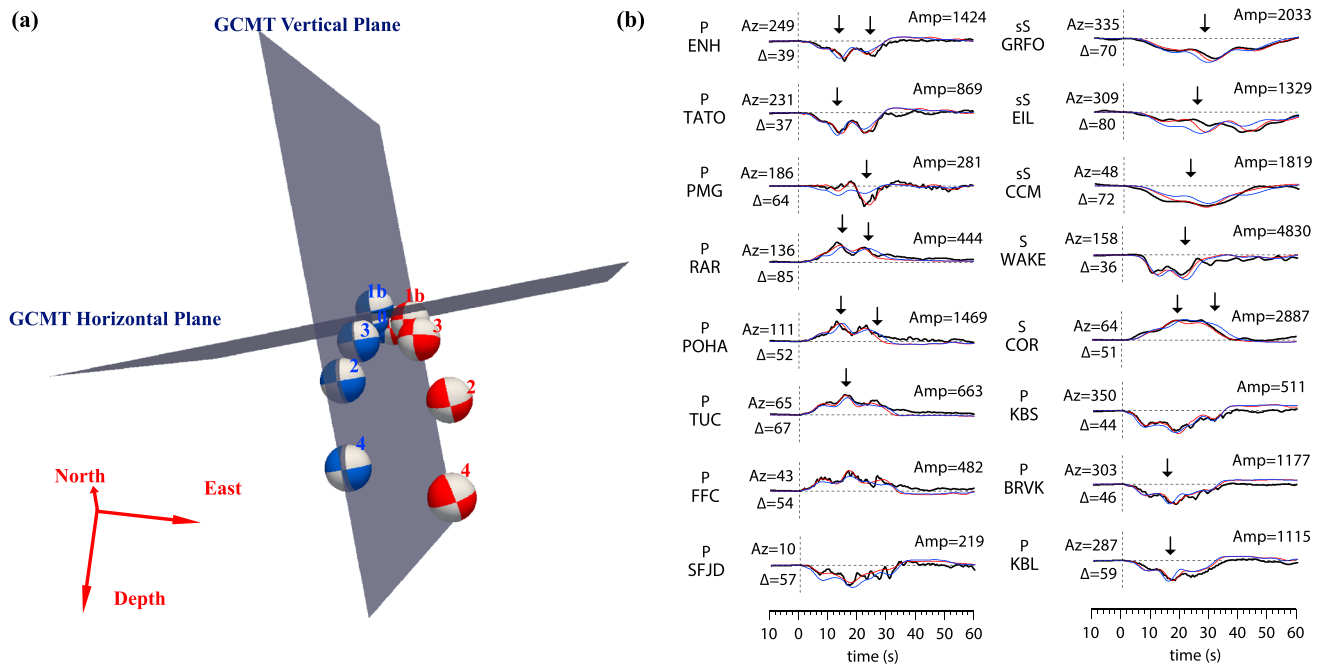


Figure 9. (a) Three-dimensional spatial distribution of focal mechanisms of the best fitting model (red beach balls) and the inverted model compelling the subevents on the GCMT subvertical plane (blue beach balls), labeled with sequence of their occurring time, along with the focal planes (gray planes) in the GCMT solution. (b) Selected seismograms (black traces) comparing with synthetics (red traces) predicted by the best fitting source model (Table 1, red beach balls in Figure 9a) and synthetics (blue traces) predicted by the best fitting source model (Table S4, blue beach balls in Figure 9a) on the GCMT subvertical plane. The waveform fitting of all used stations is shown in Figure S5.

The second test is to confine the seismic energy on the GCMT subvertical plane. The synthetics of such inversion results (Figure 9a and Table S4) cannot match the observations in both arrival times and radiation patterns of major energy groups. The mismatches are due to the fact that the assumed subvertical plane of rupture prescribes the seismic source to move in a way that the predicted energy associated with the second and fourth pulses would not fit the azimuthal dependence of their arrival times and amplitudes in the *P* and *pP* observations. The seismic source for the second and fourth pulses are required to move east and deeper, while the GCMT subvertical plane inversion places the energy north and shallower resulting in the synthetic misfits to the observations. The arrival times between the best fitting model and the model constrained on the GCMT subvertical plane are almost the same around 0° and 180°. The most obvious misfits are presented at stations around 90° and 270°. The major groups of energy arrive earlier in the observed *P* waveforms than in the synthetics at stations POHA, KIP, JOHN, and RAR, and later at stations ENH, CHTO, LSA, KBL, MAKZ, AAK, and BRVK (Figures 9b and S5a). The mismatch of arrival times is also evident in the *S* waveforms at stations PFO, COR, and WAKE (Figure S5c), and the *sS* waveforms at stations EIL, KIEV, and GRFO (Figure S5d). The misfits of radiation pattern are evident in *P* waveform at station PMG and in *sS* waveforms at stations ANMO and TUC (Figures 9b and S5).

Our third test is to adopt a plane that best fits the spatial distribution of the subevents from the multiple source inversion. The plane has a strike of 350° and a dip of 65° (Figure 10a and Table S5). While the predicted arrival times of major groups of the energy fit the observations reasonably well, the predicted amplitudes do not fit the data (Figures 10b and S6). This is due to the fact that such a plane would prescribe focal mechanisms that would not fit the azimuthal variations of seismic amplitudes in the data. These inversion tests indicate that the fitting of the seismic data cannot be compromised with rupture on a plane.

6.3. Effects of Attenuation

Earth's attenuation would result in broadening of wave shapes and apparent "delay" of the peaks of seismic energy (Figure 11a). However, the different durations observed between *pP* and *P* waveforms (Figure 3a) are not caused by the effect of attenuation. We test various attenuation models by changing path-integrated

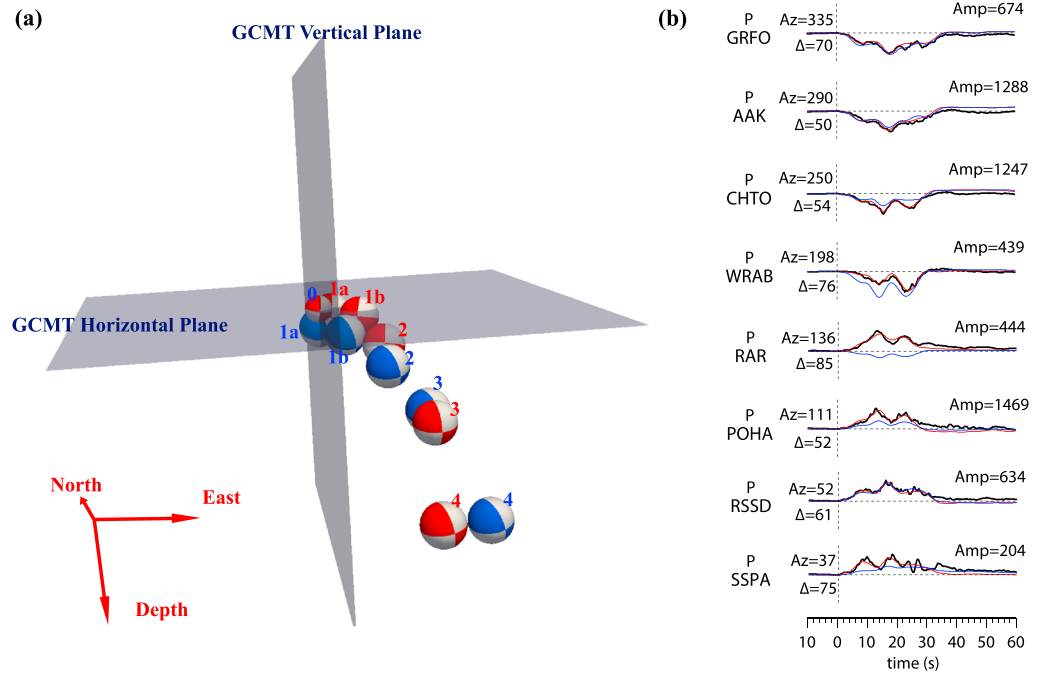


Figure 10. (a) Three-dimensional spatial distribution of focal mechanisms of the best fitting model (red beach balls) and the inverted model compelling the subevents on the plane that best connects the best fitting model (blue beach balls), labeled with sequence of their occurring time, along with the focal planes (gray planes) in the GCMT solution. (b) Selected seismograms (black traces) comparing with synthetics (red traces) predicted by the best fitting source model (Table 1, red beach balls in Figure 10a) and synthetics (blue traces) predicted by the best fitting source model (Table S5, blue beach balls in Figure 10a) on a plane that best connects the inferred subevents in Table 1. The waveform fitting of all used stations is shown in Figure S6.

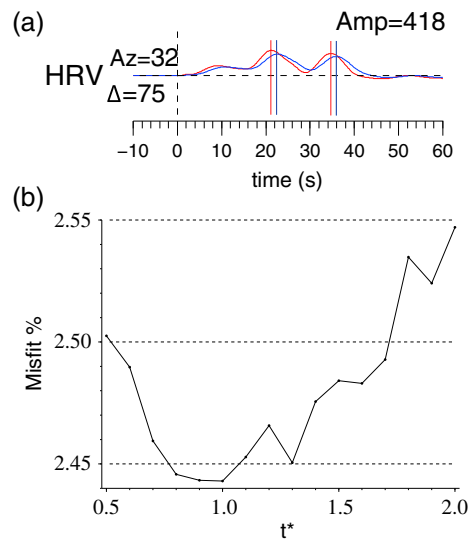


Figure 11. (a) Synthetics (red traces) of *pP* waves attenuated by $t^* = 1.45$ based on the PREM model and synthetics (blue traces) of *pP* waves attenuated by $t^* = 2.61$ (1.8 times of PREM values) predicted by the best fitting source model (Table 1). The red and blue lines mark the peaks of subevents 2 and 4. (b) The misfits (RMS) of amplitudes between the data and synthetics predicted based on the best fitting model by varying t^* of *pP* phase from 0.5 to 2.0 times of the PREM values.

attenuation t^* value from 0.5 to 2 times of PREM values for *pP* synthetics. The misfits do not vary much with t^* values ranging from 0.6 to 1.7 times of PREM values (Figure 11b). When t^* reaches 1.8 times of PREM values, misfits start to increase rapidly (Figure 11b). With this attenuation structure, the apparent delay of the peaks of individual pulses of *pP* waves is at most 1.5 s (Figure 11a), which is significantly smaller than 7–8 s observed in the *P* and *pP* data (Figure 3). More importantly, the predicted time differences between the peaks of different subevent energy, which are used to infer the depth separations between the subevents, differ at most by 0.2 s between different attenuation models. (Figure 11a). Therefore, the depth extension among subevents 1–4 is little affected by attenuation. We conclude that the observed time difference between *P* and *pP* wave energy is caused by the depth extension of seismic source.

6.4. Three-Dimensional Effect of Slab Structure

It is well known that a sharp structure of a subducted slab may have profound effects on wave propagation [Chen *et al.*, 2007]. In some specific slab geometry, the sharp feature of the slab structure may exhibit multipath effects, producing an additional pulse at some azimuths. The extent of such effects would likely vary from slab to slab. However, if such effect exists, the additional pulse in the propagational effects could be mistaken as a subevent or

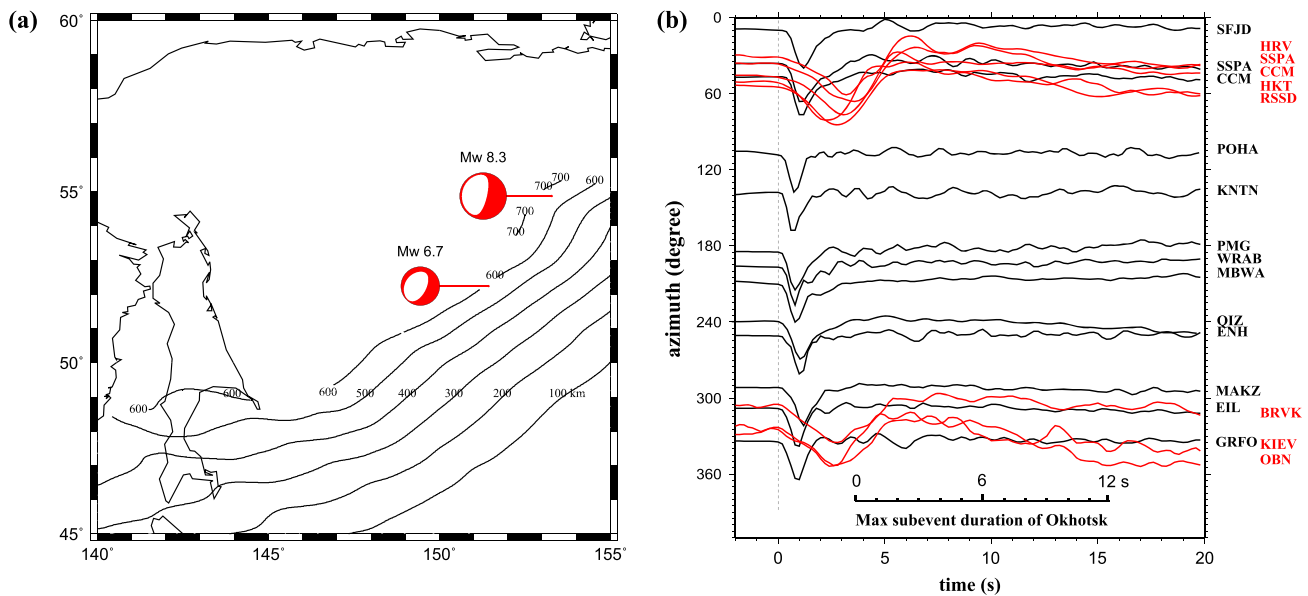


Figure 12. (a) Location and focal mechanisms (red beach balls) of the main shock and a nearby aftershock. The depth contours labeled with slab depth are from the USGS Slab 1.0 model. (b) Observed vertical *P* (black traces) and *pP* (red traces) displacement seismograms of the aftershock as a function of azimuth.

contaminate our results during the inversion. For the seismic data used in the present study, the three-dimensional (3-D) propagational effects due to the slab structure are minor. This is demonstrated in a nearby aftershock data recorded at these stations (Figure 12a). The *P* waves of the aftershock exhibit a simple pulse with a duration of 2 s in four quadrants (Figure 12b). No obvious additional pulses are observed within the range of time separation between the inverted subevents for the main shock (Figure 12b). Same waveform characteristics are observed for the *pP* waves as well, although their main phases exhibit a longer duration, which may be due to either stronger attenuation or down-dip rupture directivity. We thus conclude that the 3-D slab effect is minor in our data and does not affect our inversion result of the Okhotsk earthquake.

6.5. Horizontal Extension of the Energy Propagation

The spatial distribution of the source process in this study represents the centroid location of each subevent. Therefore, the horizontal extension of 64 km in this study is roughly consistent with the previous study [Ye *et al.*, 2013], and smaller than 100 km reported by the others [Wei *et al.*, 2013; Zhan *et al.*, 2014]. The discrepancy arises from the fact that different types of data used between the studies. The result of the previous study is inferred from waveform fitting of *P* wave data only, while our result is obtained based on waveform fitting of both *P* and *S* wave data. While a lateral extent larger than 100 km would still produce reasonably good fit to the *P* wave data, it would generate an *S* wave energy moveout different from the observed data. We present an example of synthetic test to illustrate the effect, by compelling the parameter “*dn*” of subevent 4 to be larger than 90 km south to the earthquake initiation point (Figure 13a and Table S6). While the observed *P* waveforms can still be reasonably fit by the model (Figures 13b and S7a), significant misfits are apparent in *S* waves at stations SFJD, IVI, CLF, KBS, and DAG (Figures 13b and S7c). The seismic energy generated by subevent 4 exhibits a very different moveout from the data (Figures 13b and S7c). And some misfits are exhibited in *pP* and *sS* as well (Figures S7b and S7d).

7. Possible Interpretations

The inferred source process does not prefer phase transformational faulting. The transformational faulting events would occur in the interface of the metastable olivine-spinel wedge, so the orientation of the wedge would follow the subevent locations as in Figure 5a. It is unlikely that the metastable wedge would possess that kind of geometry.

It is interesting to note that the inferred subevents could be classified into two groups with similar focal mechanisms, with subevents 0, 1a, 1b, and 3 forming one and subevents 2 and 4 the other. The spatiotemporal

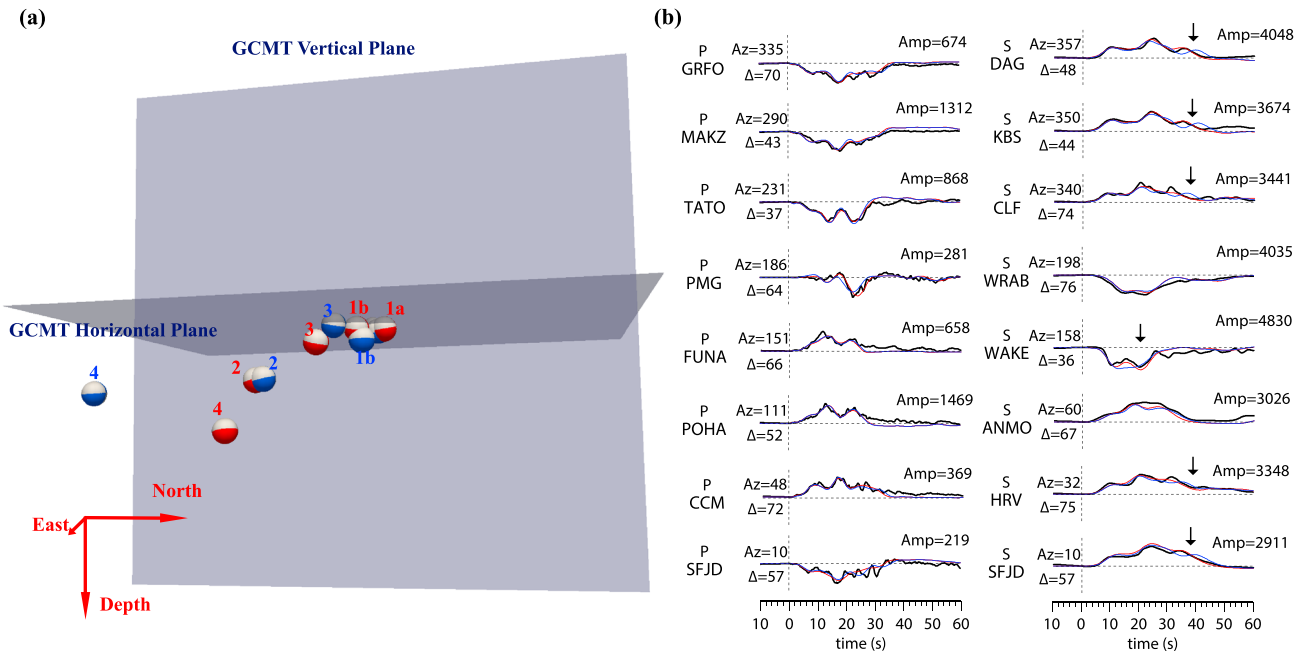


Figure 13. (a) Three-dimensional spatial distribution of focal mechanisms of the best fitting model (red beach balls) and the inverted model compelling subevent 4 to 90 km south to the initiation of the earthquake (blue beach balls), labeled with sequence of their occurring time, along with the focal planes (gray planes) in the GCMT solution. (b) Selected seismograms (black traces) comparing with synthetics (red traces) predicted by the best fitting source model (Table 1, red beach balls in Figure 13a) and synthetics (blue traces) predicted by the best fitting source model (Table S6, blue beach balls in Figure 13a) by compelling subevent 4 to 90 km south to the initiation of the earthquake. Arrows point to the misfits of the blue traces. The waveform fitting of all used stations is shown in Figure S7.

distribution of the subevents could be explained with rupture on two planes approximately orthogonal to each other with one subhorizontal plane hosting the rupture of subevents 0, 1a, 1b, and 3 and one subvertical plane hosting the rupture of subevents 2 and 4 (Figure 14). In this scenario, the earthquake is initiated on the subhorizontal plane with a rupture velocity of 2 km/s and a lateral dimension of 27 km. At 12 s during the subhorizontal rupture, a downward rupture is triggered on a near subvertical plane 24 km southeast of the subhorizontal rupture, with a rupture velocity of 2 km/s. It is also interesting to note that such rupture process

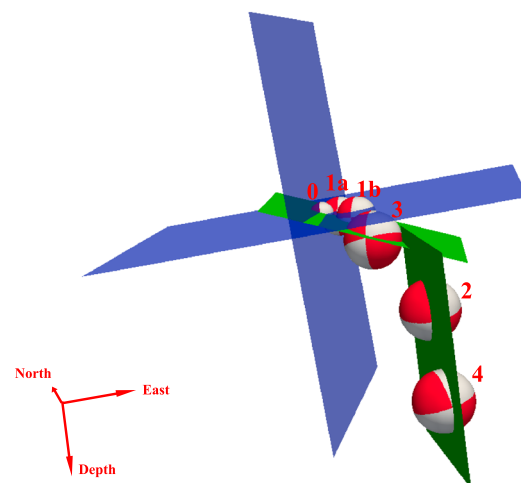


Figure 14. A two-plane rupture model (green planes) that could accommodate the locations and focal mechanisms of the inferred subevents (red beach balls labeled with sequence of their occurring times). Two GCMT fault planes are presented as blue planes.

would resemble that of the 11 April 2012 great earthquake in the Indian Ocean [Meng *et al.*, 2012; Yue *et al.*, 2012] and may represent reactivation at depth of such a preexisting type of fault system observed in oceanic lithosphere before subduction. However, none of the aftershock locations fits into these two possible rupture planes (Figure 5a), making this two-plane rupture explanation unlikely.

The source process and foreshocks/aftershocks distribution indicate that the earthquake is a combination of smaller earthquakes occurring in close space and time. The close proximity and timing of the subevents suggest a cascading failure of the region during this earthquake, with some triggering mechanisms between the subevents. The likely triggering forces are the static or dynamic stress generated by the preceding subevent(s) [Hill, 2008; Tibi *et al.*, 2003].

The inferred source process of the Okhotsk earthquake is more consistent with a cascading failure of shear thermal instabilities in the region.

Shear thermal instability is a failure due to positive feedback between viscous heating and temperature-dependent rheology [Hobbs and Ord, 1988; Kelemen and Hirth, 2007]. Such feedback system is naturally influenced by perturbation of stress, providing a mechanism for a cascading failure in a region. While a preexisting zone of weak rheology is not a requirement for shear thermal instability to occur, it would prescribe the instability to occur along its orientation. Such weak zones are known to exist within the subducted slab, due to either past faulting before subduction [Silver *et al.*, 1995] or existence of preexisting fine-grained shear zones [Kelemen and Hirth, 2007]. The focal mechanisms of the subevents thus could reflect the orientations of the preexisting weak zones. In short, the Okhotsk earthquake can be best explained by a cascading series of failures in a region of preexisting weak zones, with the perturbation of stress generated by a shear instability triggering another and the orientations of the preexisting weak zones controlling the focal mechanisms of these instabilities.

8. Conclusion

We investigate the source process of the 24 May 2013 *M*_w 8.3 Okhotsk deep earthquake based on waveform modeling of *P*, *pP*, *SH*, and *sSH* wave data. The seismic source directivity analyses and multiple source inversion results suggest that the earthquake can be modeled by six subevents, with a horizontal extension of 64 km and a depth extension of 35 km. The model resolutions are $\pm 2^\circ$ for each focal parameter, ± 0.5 s for *dt*, and ± 4 km for location. Synthetics tests further indicate that the seismic data cannot be explained by rupture on a single plane. The spatial distribution of the foreshocks/aftershocks also does not fit into a plane or two planes with the inferred subevents. These results suggest that the earthquake is a combination of smaller earthquakes close in time and space. We suggest that the earthquake can be best explained by a cascading failure of shear instability within preexisting weak zones in the region, with the perturbation of stress generated by a shear instability triggering another.

Acknowledgments

We thank the Editors and two anonymous reviewers for the constructive suggestions, which improved the paper significantly. The seismic data are downloaded from the Incorporated Research Institutions for Seismology (IRIS). The work is supported by NSF EAR1214215 and the Chinese Academy of Sciences and State Administration of Foreign Experts Affairs International Partnership Program for Creative Research Teams.

References

- Antolik, M., D. Dreger, and B. Romanowicz (1996), Finite fault source study of the great 1994 deep Bolivia earthquake, *Geophys. Res. Lett.*, *23*(13), 1589–1592, doi:10.1029/96GL00968.
- Antolik, M., D. Dreger, and B. Romanowicz (1999), Rupture processes of large deep-focus earthquakes from inversion of moment rate functions, *J. Geophys. Res.*, *104*(B1), 863–894, doi:10.1029/1998JB900042.
- Chen, M., J. Tromp, D. Helmberger, and H. Kanamori (2007), Waveform modeling of the slab beneath Japan, *J. Geophys. Res.*, *112*, B02305, doi:10.1029/2006JB004394.
- Dziewonski, A. M., and D. L. Anderson (1981), Preliminary reference Earth model, *Phys. Earth Planet. Inter.*, *25*(4), 297–356, doi:10.1016/0031-9201(81)90046-7.
- Estabrook, C. H. (2004), Seismic constraints on mechanisms of deep earthquake rupture, *J. Geophys. Res.*, *109*, B02306, doi:10.1029/2003JB002449.
- Green, H. W. (2007), Shearing instabilities accompanying high-pressure phase transformations and the mechanics of deep earthquakes, *Proc. Natl. Acad. Sci. U.S.A.*, *104*(22), 9133–9138, doi:10.1073/pnas.0608045104.
- Green, H. W., and H. Houston (1995), The mechanisms of deep earthquakes, *Annu. Rev. Earth Planet. Sci.*, *23*, 169–213, doi:10.1146/annurev.ea.23.050195.001125.
- Hayes, G. P., D. J. Wald, and R. L. Johnson (2012), Slab1.0: A three-dimensional model of global subduction zone geometries, *J. Geophys. Res.*, *117*, B01302, doi:10.1029/2011JB008524.
- Helmberg, D. V. (1968), The crust-mantle transition in Bering Sea, *Bull. Seismol. Soc. Am.*, *58*(1), 179–214.
- Hill, D. P. (2008), Dynamic stresses, Coulomb failure, and remote triggering, *Bull. Seismol. Soc. Am.*, *98*(1), 66–92, doi:10.1785/0120070049.
- Hobbs, B. E., and A. Ord (1988), Plastic instabilities—Implications for the origin of intermediate and deep-focus earthquakes, *J. Geophys. Res.*, *93*(B9), 10,521–10,540, doi:10.1029/JB093iB09p10521.
- Ji, C., D. J. Wald, and D. V. Helmberger (2002), Source description of the 1999 Hector Mine, California, earthquake, Part II: Complexity of slip history, *Bull. Seismol. Soc. Am.*, *92*(4), 1208–1226, doi:10.1785/0120000917.
- Jung, H., H. W. Green, and L. F. Dobrzinetskaya (2004), Intermediate-depth earthquake faulting by dehydration embrittlement with negative volume change, *Nature*, *428*(6982), 545–549, doi:10.1038/nature02412.
- Kanamori, H., D. L. Anderson, and T. H. Heaton (1998), Frictional melting during the rupture of the 1994 Bolivian earthquake, *Science*, *279*(5352), 839–842, doi:10.1126/science.279.5352.839.
- Kelemen, P. B., and G. Hirth (2007), A periodic shear-heating mechanism for intermediate-depth earthquakes in the mantle, *Nature*, *446*(7137), 787–790, doi:10.1038/nature05717.
- Kennett, B. L. N., and E. R. Engdahl (1991), Traveltimes for global earthquake location and phase identification, *Geophys. J. Int.*, *105*(2), 429–465, doi:10.1111/j.1365-246x.1991.tb06724.x.
- Kirby, S. H. (1987), Localized polymorphic phase-transformations in high-pressure faults and applications to the physical-mechanism of deep earthquakes, *J. Geophys. Res.*, *92*(B13), 13,789–13,800, doi:10.1029/JB092iB13p13789.
- Kirby, S. H., S. Stein, E. A. Okal, and D. C. Rubie (1996), Metastable mantle phase transformations and deep earthquakes in subducting oceanic lithosphere, *Rev. Geophys.*, *34*(2), 261–306, doi:10.1029/96RG01050.
- Meade, C., and R. Jeanloz (1989), Acoustic emissions and shear instabilities during phase-transformations in Si and Ge at ultrahigh pressures, *Nature*, *339*(6226), 616–618, doi:10.1038/339616a0.
- Meade, C., and R. Jeanloz (1991), Deep-focus earthquakes and recycling of water into the Earth's mantle, *Science*, *252*(5002), 68–72, doi:10.1126/science.252.5002.68.

- Meng, L., J. P. Ampuero, J. Stock, Z. Duputel, Y. Luo, and V. C. Tsai (2012), Earthquake in a maze: Compressional rupture branching during the 2012 *Mw* 8.6 Sumatra earthquake, *Science*, *337*(6095), 724–726, doi:10.1126/science.1224030.
- Ogawa, M. (1987), Shear instability in a viscoelastic material as the cause of deep-focus earthquakes, *J. Geophys. Res.*, *92*(B13), 13,801–13,810, doi:10.1029/JB092iB13p13801.
- Scholz, C. H. (2002), *The Mechanics of Earthquakes and Faulting*, 2nd ed., Cambridge Univ. Press, Cambridge, New York, Melbourne.
- Silver, P. G., S. L. Beck, T. C. Wallace, C. Meade, S. C. Myers, D. E. James, and R. Kuehnel (1995), Rupture characteristics of the deep Bolivian earthquake of 9 June 1994 and the mechanisms of deep-focus earthquakes, *Science*, *268*(5207), 69–73, doi:10.1126/science.268.5207.69.
- Tibi, R., D. A. Wiens, and H. Inoue (2003), Remote triggering of deep earthquakes in the 2002 Tonga sequences, *Nature*, *424*(6951), 921–925, doi:10.1038/nature01903.
- Wei, S. J., D. Helmberger, Z. W. Zhan, and R. Graves (2013), Rupture complexity of the *Mw* 8.3 sea of okhotsk earthquake: Rapid triggering of complementary earthquakes?, *Geophys. Res. Lett.*, *40*, 5034–5039, doi:10.1002/grl.50977.
- Wen, L. (2006), Localized temporal change of the Earth's inner core boundary, *Science*, *314*(5801), 967–970.
- Wiens, D. A., J. J. McGuire, and P. J. Shore (1993), Evidence for transformational faulting from a deep double seismic zone in Tonga, *Nature*, *364*(6440), 790–793, doi:10.1038/364790a0.
- Wiens, D. A., J. J. McGuire, P. J. Shore, M. G. Bevis, K. Draunidalo, G. Prasad, and S. P. Helu (1994), A deep earthquake aftershock sequence and implications for the rupture mechanism of deep earthquakes, *Nature*, *372*(6506), 540–543, doi:10.1038/372540a0.
- Ye, L., T. Lay, H. Kanamori, and K. D. Koper (2013), Energy release of the 2013 *Mw* 8.3 Sea of Okhotsk earthquake and deep slab stress heterogeneity, *Science*, *341*(6152), 1380–1384, doi:10.1126/science.1242032.
- Yue, H., T. Lay, and K. D. Koper (2012), En echelon and orthogonal fault ruptures of the 11 April 2012 great intraplate earthquakes, *Nature*, *490*(7419), 245–249, doi:10.1038/nature11492.
- Zhan, Z., H. Kanamori, V. C. Tsai, D. V. Helmberger, and S. Wei (2014), Rupture complexity of the 1994 Bolivia and 2013 Sea of Okhotsk deep earthquakes, *Earth Planet. Sci. Lett.*, *385*, 89–96, doi:10.1016/j.epsl.2013.10.028.